Traveling Waves of Calcium in Pancreatic Acinar Cells: Model Construction and Bifurcation Analysis

James Sneyd[1], Andrew LeBeau[2] and David Yule[3].

6 October, 1998

[1]Department of Mathematics, University of Michigan, 525 East University Avenue, Ann Arbor, MI, 48109-1109, USA. jsneyd@math.lsa.umich.edu. To whom correspondence should be addressed.

[2]Mathematical Research Branch, NIH, 9190 Rockville Pike, Suite 350, Bethesda, MD, USA

[3]Department of Physiology, University of Michigan, Ann Arbor, MI. Present address: Department of Pharmacology and Physiology, University of Rochester, School of Medicine and Dentistry, Rochester, NY, USA

Running Head: Traveling Ca^{2+} Waves

Keywords: Calcium waves, mathematical model, traveling waves, bifurcation theory, inositol trisphosphate receptor, homoclinic bifurcations, T-point, pancreatic acinar cells

Abstract

We construct and study a model for intracellular calcium wave propagation, with particular attention to pancreatic acinar cells. The model is based on a model of the inositol trisphosphate (IP_3) receptor, which assumes that calcium modulates the binding affinity of IP_3 to the receptor. Two versions of the model, one simpler than the other, are studied numerically. In both versions, solitary waves in the excitable regime arise via homoclinic bifurcations in the traveling wave equations. As the background concentration of IP_3 is increased, the wave speed increases, and for some values of the IP_3 concentration, the initial pulse gives rise to secondary pulses that travel in both directions. This can give rise to irregular spatio-temporal behavior, or to trains of pulses. In the simpler model, these secondary waves are related to the presence of a T-point, a heteroclinic cycle, and an associated spiral of homoclinic orbits, which terminate the branch of homoclinic orbits.

1 Introduction

Traveling waves of increased cytoplasmic calcium (Ca^{2+}) concentration have been observed in many cell types, and are widely believed to be one important mechanism by which a group of cells, or a single large cell, is able to coordinate behavior over a large region (Thomas *et al.*, 1996). Thus, Ca^{2+} waves, both within a single cell, and between cells, have been studied in detail by both experimentalists and theoreticians, and there exists a large body of work on the mechanisms underlying such wave propagation.

The pancreatic acinus is a particularly interesting system in which to study Ca^{2+} waves (Nathanson *et al.*, 1992; Kasai, 1995; Yule *et al.*, 1996; Pfeiffer *et al.*, 1998). Firstly, the pancreatic acinar cell is electrically non-excitable, and the Ca^{2+} wave results (at least in large part) from the release of Ca^{2+} from the endoplasmic reticulum. Secondly, each acinus consists of a number of cells arranged in ring around a central duct, and the Ca^{2+} wave travels from cell to cell around this ring in a characteristic fashion (Yule *et al.*, 1996). The function of this intercellular Ca^{2+} wave is not entirely clear, although it appears to increase the efficiency of enzyme secretion of the acinus, presumably by coordinating the secretion of each individual cell with that of its neighbors. Thirdly, different agonists cause different wave responses (Lawrie *et al.*, 1993; Thorn *et al.*, 1993). This, in turn, results from the fact that different agonists cause different oscillatory responses in each individual cell. Application of intermediate doses of acetylcholine (ACh) or carbachol (CCh) causes high-frequency oscillations superimposed on a raised baseline, while application of cholecystokinin (CCK) causes baseline oscillations with a much larger period (Yule *et al.*, 1991).

Both types of agonists cause oscillations via the production of the intracellular signaling messenger inositol (1,4,5) trisphosphate (IP_3). Binding of the agonist to the cell surface receptor activates a G-protein, resulting in the activation of phospholipase C (PLC) and the subsequent production of IP_3 from phosphatidylinositol bisphosphate. IP_3 diffuses through the cell cytoplasm and binds to IP_3 receptors located on the endoplasmic reticulum (ER). These receptors, which also act as Ca^{2+} channels, then open, releasing Ca^{2+} from the ER. Subsequent inactivation of the IP_3 receptors, and removal of Ca^{2+} from the cytoplasm by membrane pumps, then returns the Ca^{2+} concentration to its resting value. If the concentration of IP_3 is in the correct range,

it can initiate a cycle of release and uptake of Ca^{2+} from the ER, resulting in Ca^{2+} oscillations.

Although different agonists cause markedly different oscillatory behavior, it is not clear how this can occur, given that they both work through the production of IP_3, and the opening of the IP_3 receptor. We addressed this question in a previous paper, in which we presented a model for Ca^{2+} oscillations in pancreatic acinar cells, and showed how the model can reproduce both long-period and short-period Ca^{2+} oscillations. Our previous model of the IP_3 receptor was based on the binding diagram shown in Fig. 1. It was assumed that the IP_3 receptor could exist in one of four different states: S - shut; O - open; I_1 - inactivated but not phosphorylated; and I_2 - inactivated and phosphorylated. The various transition rates were chosen arbitrarily to give the correct qualitative behavior. Thus, k_1 and k_2 were chosen as increasing functions of c (where c denotes $[Ca^{2+}]$), and k_3 was chosen to be a decreasing function of c. In other words, Ca^{2+} increases both the rate of receptor opening, and the rate of receptor inactivation, but decreases the rate at which the receptors recover from the inactivated state.

We also proposed that agonists such as CCK can cause much greater phosphorylation of the receptor than do agonists such as ACh, and thus shunts the receptor through the I_2 state. We showed that, if the action of the phosphatase is slow enough, this can result in long-period basline oscillations, while, if the I_2 state is bypassed, short-period, raised-baseline oscillations can occur. Thus, the model can explain both kinds of oscillations ocurring through a single type of receptor. In LeBeau *et al.* (submitted) we present experimental data to support our model, and test a number of model predictions. Here, we shall focus our attention on the model in the absence of receptor phosphorylation, and thus our results will be applicable only to waves induced by ACh or CCh. Waves in the model with phosphorylation will be studied in a later paper.

One of the least attractive aspects of our previous model was the fact that the expressions for k_1, k_2 and k_3 were not based on underlying physiological principles. They were chosen so that the model agreed with the available experimental evidence, but the functional forms were themselves arbitrary. Here, we aim to improve this aspect of the model by showing how the same model can be derived from a more detailed and realistic model of the IP_3 receptor. The basis of the new model is the

proposal (Hajnóczky and Thomas, 1997; Cardy *et al.*, 1997) that Ca^{2+} regulates the interconversion of the IP_3 receptor between two different states, one of which has a high affinity for IP_3, the other a low affinity. Here, we show that our previous model can be derived from such an assumption, and thus we provide a mechanistic interpretation of what was, originally, a more phenomenological model.

Our ultimate goal is the study of intercellular Ca^{2+} waves in a pancreatic acinus. However, before such a goal can be realised, it is necessary first to understand the properties of traveling waves in the model in a homogeneous medium. Thus, here we study the behavior of traveling waves in the model in some detail.

2 The model equations

2.1 The model of the IP_3 receptor

Instead of making the *ad hoc* assumption that the rate constants for conversion between the receptor states are functions of the Ca^{2+} concentration, we instead assume, as described above, that Ca^{2+} regulates the interconversion of the receptor between two different shut states. We also make a similar assumption for the open and inactivated states. This extended model of the IP_3 receptor is shown schematically in Fig. 2A. There are two different shut states, S and $\tilde{\mathrm{S}}$, and Ca^{2+} regulates the interconversion of the receptor between these two states. Similarly, there are two open, and two inactivated states. Since IP_3 can bind to either shut state, and convert it to an open state, the concentration of Ca^{2+} will determine the rate at which receptors are opened by IP_3. In a similar fashion, $[Ca^{2+}]$ controls the rate of receptor inactivation, and the rate of recovery from inactivation.

We now assume that the interconversion between S and $\tilde{\mathrm{S}}$ is fast compared to the conversion of S or $\tilde{\mathrm{S}}$ to O, and similarly for O and I_1. It is a simple matter to express this in terms of a formal perturbation expansion, but as this adds nothing to the conclusions we do not do so here. Letting S denote the fraction of receptors in state S, and similarly for the other states, we then obtain the relationships

$$cS = R_1\tilde{S}, \qquad cO = R_3\tilde{O}, \qquad cI_1 = R_5\tilde{I}_1, \tag{1}$$

where c denotes $[Ca^{2+}]$, and $R_i = r_{-i}/r_i$ for $i = 1, 3, 5$. Letting

$$x = S + \tilde{S}, \tag{2}$$
$$y = O + \tilde{O}, \tag{3}$$
$$z = I_1 + \tilde{I}_1, \tag{4}$$

and using the law of mass action, it follows that

$$\frac{dx}{dt} = O(k_{-1} + r_{-2}) - k_1 pS - r_2 p\tilde{S} + k_3 I_1 + r_6 \tilde{I}_1, \tag{5}$$
$$\frac{dy}{dt} = r_2 p\tilde{S} + k_1 pS - (r_{-2} + k_{-1})O - k_2 O - r_4 \tilde{O}, \tag{6}$$

where p denotes the concentration of IP_3. Note that a differential equation for z is unnecessary, as we have the conservation law $x + y + z = 1$. If we then use the constraints (1), we get

$$\frac{dx}{dt} = \phi_{-1}(c)y - p\phi_1(c)x + \phi_3(c)z, \tag{7}$$
$$\frac{dy}{dt} = p\phi_1(c)x - \phi_{-1}(c)y - \phi_2(c)y, \tag{8}$$
$$z = 1 - x - y, \tag{9}$$

where

$$\phi_1(c) = \frac{k_1 R_1 + r_2 c}{R_1 + c}, \tag{10}$$
$$\phi_{-1}(c) = \frac{(k_{-1} + r_{-2})R_3}{c + R_3}, \tag{11}$$
$$\phi_2(c) = \frac{k_2 R_3 + r_4 c}{R_3 + c}, \tag{12}$$
$$\phi_3(c) = \frac{k_3 R_5 + r_6 c}{R_5 + c}. \tag{13}$$

We shall call this model, the *three-state model*.

Clearly, (7)–(9) are equivalent to the binding diagram shown in Fig. 2B, which is itself the same as the binding diagram of the original model (Fig. 1), with the exception of the transition from the open state to the closed state, which is a function of c in the new version of the model, but a constant in the old version.

Note that, by appropriate choice of parameters, ϕ_1, ϕ_2 and ϕ_3 can be either increasing or decreasing functions of c. For instance, if $k_1 < r_2$ then $\phi_1'(c) > 0$ and thus an increase in c increases the rate of receptor opening. The parameters (Table 1) are chosen so that the present model agrees with the model of LeBeau *et al.* (submitted), and thus has the correct steady-state open probability, the correct time course for receptor activation and inactivation, and exhibits oscillations with the correct period and qualitative shape.

2.2 Steady-state open probability

We shall make the simplifying assumption that the IP_3 receptor is made up of four independent, indentical subunits, and that each subunit obeys the dynamics described above. Hence, the open probability, P, is given by $P = y^4$, with a steady value, P_s, given by

$$P_s = \left(\frac{\theta_1(c)p}{p + \theta_2(c)} \right)^4, \tag{14}$$

where

$$\theta_1 = \frac{\phi_3\phi_1}{\phi_1\phi_2 + \phi_1\phi_3}, \tag{15}$$

$$\theta_2 = \frac{\phi_3\phi_{-1} + \phi_3\phi_2}{\phi_1\phi_2 + \phi_1\phi_3}. \tag{16}$$

For the parameters used here (see Table 1) P_s is a bell-shaped function of c, and $\theta_2'(c) < 0$. The bell-shaped nature of the steady-state open probability curve is a feature that has been noted experimentally by a number of groups (Bezprozvanny and Ehrlich, 1995; Finch *et al.*, 1991; Parys *et al.*, 1992; Dufour *et al.*, 1997), and the fact that θ_2 is a decreasing function of c means that the affinity for IP_3 of the receptors increases with increasing c. This has been shown to be the case for Type III IP_3 receptors (Yoneshima *et al.*, 1997), which are the predominant receptor type in pancreatic acinar cells. We thus predict that, for Type III receptors, the peak of the bell-shaped steady-state open probability curve moves to the left as p increases. Type I IP_3 receptors have an IP_3 affinity that decreases as Ca^{2+} increases (Yoneshima *et al.*, 1997), and we have shown that, in this case, the model predicts that the peak of the steady-state open probability curve will move to the right as p increases. This is indeed what is seen experimentally (Kaftan *et al.*, 1997).

2.3 A two-variable receptor model

It will be useful to reduce the three-state model to a simpler version by assuming that opening of the receptor by IP_3 binding is a fast process compared to receptor inactivation and recovery from inactivation. This is a standard assumption used in many models (Atri *et al.*, 1993; Li and Rinzel, 1994; Keizer and DeYoung, 1994; Sneyd *et al.*, 1995; Tang *et al.*, 1996) and appears to agree well with experimental data. With this assumption we have the constraint

$$p\phi_1 x = \phi_{-1} y. \tag{17}$$

Thus, letting $h = x + y$, and recalling the conservation law which now takes the form $h + z = 1$, we get

$$\frac{dh}{dt} = \phi_3(1-h) - \left(\frac{\phi_1\phi_2 p}{\phi_1 p + \phi_{-1}}\right) h. \tag{18}$$

The open probability of the receptor is now given by

$$P = \left(\frac{ph\phi_1}{\phi_1 p + \phi_{-1}}\right)^4. \tag{19}$$

We shall call this model the *two state model*.

2.4 Incorporation into a whole-cell model

The above models of the IP_3 receptor can be incorporated into models for intracellular Ca^{2+} dynamics by assuming that Ca^{2+} can enter the cell via two pathways (through the IP_3 receptor, flux J_{receptor}, or through a generic leak from outside the cell or from the ER, J_{leak}), and is removed from the cytoplasm by the action of Ca^{2+} ATPase pumps (with flux, J_{pump}). Thus, conservation of Ca^{2+} gives

$$\frac{dc}{dt} = J_{\text{receptor}} - J_{\text{pump}} + J_{\text{leak}}. \tag{20}$$

In choosing functional forms for J_{pump} and J_{leak} we follow previous models (reviewed in Sneyd *et al.*, 1995) and assume that J_{leak} is just a specified constant, while the Ca^{2+} ATPases work in a cooperative manner, with a Hill coefficient of 2, and thus

$$J_{\text{pump}} = \frac{V_p c^2}{K_p^2 + c^2}, \tag{21}$$

for some constants V_p and K_p. The flux through the receptor is given by the open probability multiplied by some scaling factor, and thus

$$J_{\text{receptor}} = k_f y^4, \tag{22}$$

for some constant k_f. J_{leak} is assumed to be a constant. Here, we use the same parameter values as previously (LeBeau *et al.*, submitted), and these are given in Table 1.

3 Temporal oscillations

We are interested in the appearance and the behavior of oscillations as p varies. In general, p will depend on the concentration of agonist applied to the cell, and thus, in the physiological situation, is probably the most important controlling parameter. Oscillatory behavior in the models is most easily summarized by bifurcation diagrams, using p as the main bifurcation parameter. All bifurcation figures in this paper were constructed numerically using AUTO (Doedel, 1986), as implemented in *xppaut* by B. Ermentrout (http://www.pitt.edu/ phase).

In the three-state model (Fig. 3) oscillations arise via a subcritical Hopf bifurcation and disappear again via a supercritical Hopf bifurcation. The branch of unstable orbits combines with the branch of stable orbits in a saddle-node of periodics bifurcation, at which point the period of the oscillation is large, as shown in the inset to the figure.

Similar behavior occurs in the two-state model (Fig. 4). Here, the curve of steady states has folded up, forming two limit points, and this has broken the branch of periodic orbits into two different branches. On both branches, periodic orbits arise via a homoclinic bifurcation and end in a subcritical Hopf bifurcation. Note that, in both the three-state model and the two-state model, as p is increased oscillations first occur with a large period but the period then quickly decreases. This agrees well with experimental observations. It is known that although the application of ACh usually results in raised-baseline, high frequency oscillations, application of low concentrations of ACh can sometimes result in low-frequency baseline spiking (Petersen *et al.*, 1991) as predicted by both these models.

Temporal oscillations in these models, comparison with experimental data, and

experimental tests of the model are discussed in greater detail in LeBeau *et al.* (submitted). Here, we focus on the properties of traveling waves in these models.

4 Traveling waves

It is widely believed that, in many situations, traveling waves of Ca^{2+} are the result of the diffusion of Ca^{2+} between release sites. According to this hypothesis, the cell cytoplasm forms either an excitable or an oscillatory system, in either of which cases the linking of release sites by diffusion can lead to coordinated waves of high Ca^{2+} concentration. Although this is certainly not the case for all types of observed Ca^{2+} waves (Sneyd *et al.*, 1995; Jafri and Keizer, 1994) it is likely to be an accurate assumption for modeling intracellular and intercellular Ca^{2+} waves in pancreatic acinar cells (Yule *et al.*, 1996).

Thus, to study traveling waves in the model, we simply include a term describing the diffusion of Ca^{2+}, and thus, in one spatial dimension,

$$\frac{\partial c}{\partial t} = D_c \frac{\partial^2 c}{\partial x^2} + J_{\text{receptor}} - J_{\text{pump}} + J_{\text{leak}}, \tag{23}$$

where D_c is the diffusion coefficient of Ca^{2+}. In formulating the model in this way we are making some implicit assumptions. Firstly, we are ignoring multiple spatial dimensions, in the belief that a detailed understanding of wave propagation in one spatial dimension is a necessary prerequisite for the study of more complex waves. Secondly, we are ignoring the complicating effects of Ca^{2+} buffers (Wagner and Keizer, 1994; Sneyd *et al.*, 1998) and just using an effective diffusion coefficient. Until the properties of Ca^{2+} buffers in pancreatic acinar cells are characterized in more detail, this is the simplest assumption to make. Finally, we are ignoring any effects of heterogeneity within a single cell, an assumption that cannot be justified on physiological grounds, as it is well known that pancreatic acinar cells are highly polarized. However, the effects of cell polarization on wave propagation cannot be understood until wave propagation in a homogeneous medium is understood, and thus the present model should be viewed as a first step for the study of more realistic models.

4.1 Waves in the two-state model

We write the model in the traveling wave coordinate $\xi = x + st$, where s is the wave speed, and look for homoclinic orbits of the resulting set of ordinary differential equations, as such orbits correspond to isolated traveling wave solutions of the original partial differential equation. (Here, all numerically computed homoclinic orbits are actually just orbits of period 10,000. Computation of the branch of periodic orbits of period 1,000 gives the same result, which implies that the period 10,000 branch gives a good approximation of the position of the homoclinic branch. However, it should be noted that at no stage do we actually prove the existence of the homoclinic branch.) Based on previous work (Sneyd *et al.*, 1993), we expect the homoclinic orbits to arise as the limit of periodic orbits as the period tends to infinity. Hence, we begin by looking for periodic orbits arising from Hopf bifurcations in the traveling wave equations. The traveling wave equations are

$$c' = d, \tag{24}$$

$$D_c d' = sd - J_{\text{receptor}} + J_{\text{pump}} - J_{\text{leak}}, \tag{25}$$

$$sh' = \phi_3(1-h) - \left(\frac{\phi_1\phi_2 p}{\phi_1 p + \phi_{-1}}\right) h, \tag{26}$$

where a prime denotes differentiation with respect to ξ.

Some of the bifurcations of this three dimensional system are illustrated in Fig. 5. In panel A we show a curve of Hopf bifurcations (labeled HB), and three branches of homoclinic orbits (labeled HC), in the p, s phase plane. Note that here we are treating the wave speed s as a secondary bifurcation parameter. Panels B and C show magnified views of two particular areas of panel A, and we will discuss them later. The numbered crosses refer to points for which we plot the homoclinic orbits in later figures. This lets us determine how the homoclinic orbits change as we move along the different branches.

4.1.1 Behavior as $s \to \infty$

First, we see that the behavior as $s \to \infty$ is exactly that of the model in the absence of diffusion (cf. Fig. 4), as expected from the general theory (Maginu, 1985). Thus, for large values of s there are two Hopf bifurcations, and two homoclinic bifurcations. The

branch of periodic orbits that originates on the rightmost Hopf bifurcation ends in a homoclinic bifurcation on branch B, while the branch of periodic orbits arising from the leftmost Hopf bifurcation extends only a short distance to the left before ending in a homoclinic bifurcation on branch C, as shown in Fig. 4. These homoclinic orbits for large s are of little interest as they correspond to waves which, on a finite domain of physiological size, look more like spatially independent responses.

4.1.2 The branch of Hopf bifurcations

For any fixed value of s we can find the values of p at which the Hopf bifurcations occur, and then these bifurcation points can be continued in the s, p phase space to give the curve labelled HB in Fig. 5A. The most important thing about this curve is the fact that it forms a loop, and thus has two limit points (labeled LP1 and LP2). These limit points exist only because the curve of steady states itself has two limit points (i.e., it is an S-shaped curve) as shown in Fig. 4. The limit points of the HB curve must necessarily coincide with the limit points of the steady-state curve, i.e., the points LP are when a Hopf bifurcation occurs at a limit point of the steady state curve. For values of p between LP1 and LP2, there are three steady-state solutions.

When the Hopf bifurcation coincides with the limit point of the steady state curve we get a codimension two bifurcation, with eigenvalues $0 \pm 0.137i$ and 0 at LP1, and eigenvalues $0 \pm 0.191i$ and 0 at LP2. Analysis of such codimension two bifurcations is a standard part of textbooks on dynamical systems (for example Wiggins, 1990). Here, we merely note that at LP1 there exists a branch of homoclinic orbits (branch A) which exists on both sides of LP1, a branch of Hopf bifurcations (HB), and a branch of saddle-node bifurcations (not shown explicitly in the diagram). The same occurs for LP2, except that now the branch of homoclinic orbits (branch C) appears to exist only on one side of LP2, and it has a markedly different character from the homoclinic branch close to LP1. We shall discuss this in more detail later.

4.1.3 Homoclinic branch A: upper part

For intermediate values of s, the branch of periodic orbits that originates on the rightmost branch of Hopf bifurcations ends in a homoclinic bifurcation on branch A. This is illustrated in Fig. 6, where we show the amplitude and period of the periodic orbits as

functions of p, for fixed $s = 12$. The dashed line denotes the curve of steady states, and the solid lines denote the maximum and minimum of c over a periodic orbit. Stability is not indicated, as the stability of the periodic waves in the traveling wave variable is unrelated to the stability of the waves as solutions of the partial differential equation. The period is shown in the inset.

When $s = 12$, the homoclinic orbit on branch A occurs at a saddle focus, with eigenvalues $-0.075 \pm 0.0647i$ and 0.537. This is the classic situation first studied by Sil'nikov (1965) and then by Glendinning and Sparrow (1984). As expected from the work of Glendinning and Sparrow (1984), close to the homoclinic orbit the period is not a single-valued function of p; instead, there are an infinite number of limit points (of which only the first few are apparent from the inset in the figure) which occur as the branch of periodic orbits winds back and forth across the value of p at which the homoclinic bifurcation occurs. Again, we are not too concerned with the complexities of the flow around the saddle-focus homoclinic orbit, as numerical simulations of the PDEs indicate that only the principal homoclinic orbit is important, as we shall show later.

The upper part of homoclinic branch A ends at a T-point (Glendinning and Sparrow, 1986) a point where a heteroclinic cycle exists between a saddle point and a saddle focus. This is shown in magnified view in Fig. 5B. Note that this is possible because once p gets to the right of LP1, there are three steady states.

In Fig. 7 we show how the homoclinic orbit changes as we move along branch A towards the T-point. At point 1 (the place of which is shown in Fig. 5A) the homoclinic orbit is a simple loop, with only a small oscillatory tail which results from the fact that it occurs at a saddle focus as described above. However, as p increases, two more steady states appear in a saddle-node bifurcation; one is a saddle point, the other is an unstable node. The homoclinic orbit now makes a brief excursion to the saddle point before eventually returning to the saddle focus to complete the cycle (orbit 2; also see Fig. 5B). Moving closer to the T-point (orbit 3), the homoclinic cycle now travels close to the saddle point, spending a long time in its vicinity, before finally returning to the saddle focus. Note that the oscillatory nature of the saddle focus is much more apparent in orbits 2 and 3.

4.1.4 The T-point and homoclinic branch B

Right at the T-point the homoclinic orbit on branch A intersects the saddle point, forming a heteroclinic cycle, as shown in Fig. 8. Panel A shows the whole cycle, while panel B shows a magnified view of the cycle in the vicinity of the saddle focus (SF) and the saddle point (SP). Such T-points have been studied by Glendinning and Sparrow (1986) who showed that at such points there exists a spiral of homoclinic orbits in the appropriate two-dimensional phase space. As expected, we see such a spiral of homoclinic orbits (branch B, as shown in Fig. 5B).

It thus follows that, at the T-point, there are two branches of homoclinic orbits, one following a spiral path, the other a linear one. It is interesting to see how such branches can occur. From the analysis of Glendinning and Sparrow (1986) we can see that the spiral of homoclinic orbits occurs when the homoclinic orbits begin and end at the saddle point SP. The spiral nature results from the spiral nature of the trajectories in the vicinity of the saddle focus SF. Speaking loosely, the heteroclinic cycle has "fallen off" the saddle focus, but remained "attached" to the saddle point, resulting in a homoclinic orbit that begins and ends at SP. This results in the series of homoclinic orbits shown in Fig. 9, where we show orbits 4,5 and 6, as labeled in Fig. 5A and B.

However, the heteroclinic cycle can also be broken by "falling off" the saddle point, but remaining attached to the saddle focus. In this case, the construction of the Poincaré map is slightly different from that given by Glendinning and Sparrow (1986), but it is easy to show that this results in a branch of homoclinic orbits that follows a linear path in phase space. These homoclinic orbits begin and end at the saddle focus, and were illustrated previously (Fig. 7).

Note that as we move along branch B away from the T-point, the initial oscillations (that are caused by the orbit moving close to the saddle focus) disappear, until at high values of s (orbit 4 for instance) the homoclinic orbit looks just like the high-period orbits observed close to the Hopf bifurcation in the model without diffusion. Thus, once the speed is high enough, these homoclinic orbits just look like spatially independent oscillations.

4.1.5 Homoclinic branch A: lower part

The lower part of the homoclinic branch A passes through the limit point LP1. As p increases along this part of branch A, the amplitude of the homoclinic orbit decreases, and it develops an oscillatory tail (Fig. 10). We were unable to track this branch past point 9, but we conjecture that the amplitude dies away to zero at a point close to point 9. Both homoclinic orbits 7 and 8 arise from branches of periodic orbits that themselves arise at Hopf bifurcations. In Fig. 11 we plot bifurcation diagrams for three fixed values of s. The dotted line denotes the curve of steady states, while the solid lines denote the maximum and minimum amplitude of the periodic orbits. The panels on the right show the period of the orbits as a function of p. When $s = 5.9$ (top panels) there are two Hopf bifurcations, and the consequent branches of periodic orbits both end in homoclinic bifurcations (at different values of p). As s decreases, the homoclinic bifurcations move closer together (middle panels), until at $s = 5.5$ (bottom panels) the homoclinic bifurcations have merged and the two branches of periodic orbits form a continuous loop, on which the period remains bounded.

4.1.6 Homoclinic branch C

The final branch that we shall discuss is branch C. For large values of s, branch C arises as the limit of the branch of periodic waves that begins at the leftmost Hopf bifurcation. As s decreases, branch C begins to fold up (Fig. 5C), the folds gradually becoming smaller until branch C intersects the curve of Hopf bifurcations at LP2. This behavior has been observed before by Balmforth *et al.* (1994), who concluded that the bends in the branch of homoclinic orbits correspond to homoclinic orbits that make multiple loops around one of the other steady states before returning to the starting point. Our results agree with this conclusion. Orbit 10 goes once around another steady state before returning to rest (Fig. 12), but orbit 11, which occurs on branch C after the first fold, winds around the other steady state twice before returning to rest. Orbit 12, which occurs after 3 further folds in branch C makes approximately three loops around the other steady state before returning to rest.

4.1.7 Waves in the two-state model PDEs

Our ultimate goal is, of course, the study of waves in the partial differential equations, and for physiological reasons we are only interested in those which are stable, and which can be generated by physiological initial conditions. Thus, not all the waves found above are physiologically significant. The ones that are can be found by direct solution of the PDEs, holding p fixed over the entire domain, and using a pulse of c as an initial condition. The PDEs were solved using a simple implicit scheme with no-flux boundary conditions on a domain of length 800 μm. Different numbers of grid points (ranging from 200 to 1000) were used, and there were no significant differences between the runs. For all the runs, at $t = 0$ c was set equal to 0.5 on the leftmost 10 grid points.

When $p = 0.22$ a stable traveling wave is initiated and moves across the domain at a speed of just over 10 $\mu\mathrm{m\,s}^{-1}$ (Fig. 13, top panel). Comparison of this wave with trace 1 of Fig. 7 shows that this traveling wave corresonds to a homoclinic orbit lying on branch A of Fig. 5. As p increases, numerical simulations with the same initial condition continue to pick out homoclinic orbits on branch A. Thus, for instance, when $p = 0.2432$ the traveling wave has developed an oscillatory tail, which is caused by the homoclinic orbit traveling close to the saddle point before returning to the saddle focus, as discussed above. As p increases still further, the orbit spends more time in the vicinity of the saddle point (Fig. 7, orbits 2 and 3), and thus the tail of the traveling wave becomes more pronounced. However, once p is large enough, something interesting happens to the traveling wave in the PDE. If the saddle point is far enough away from the saddle focus, the tail of the traveling wave can actually be pulled above the threshold for wave initiation, and thus the tail of the traveling wave will itself initiate a secondary traveling wave, which now travels in both direction. The beginning of this process can be seen in the bottom panel of Fig. 13. At $t = 20$ s, the traveling wave has a pronounced trailing hump, which gets bigger as time increases. By $t = 38$ s, the trailing hump has just increases over the threshold of wave initiation, and by $t = 40$ s a secondary wave is being initiated.

Because the secondary wave travels in both directions, it is easiest to study this wave behavior in the x, t plane, using a grayscale to indicate the value of c (Fig. 14). Note that since t increases in the downward direction, and x increases from left to

right, a line sloping down from left to right corresponds to a wave traveling from left to right across the domain, while a line sloping down from right to left corresponds to a wave traveling in the opposite direction. When $p = 0.24326$ the initial wave appears as the uppermost line sloping from left to right. However, at about 38 s a secondary wave appears and travels in both directions. When each wave reaches the boundary the tail of the wave is forced over the threshold, which initiates further waves and so on. When $p = 0.24327$ the secondary wave is initiated sooner (as the saddle point has now moved slightly further away from the saddle focus, and thus acts to pull the trajectory over the threshold sooner), and each secondary wave initiates its own secondary wave. Hence, we get a cascade of wave initiation, until at large times the domain contains a large number of waves moving in both directions. Looked at in the time domain, the waves appear disordered and irregular. For even larger values of p each secondary wave is initiated so soon after the primary wave, that the secondary waves all appear first at the boundary. Thus, all the waves in the domain travel in the same direction, forming a periodic plane wave. When $p = 0.2434$, branch A of homoclinic orbits no longer exists (see Fig. 5B). However, the underlying kinetics are now self-oscillatory (i.e., they have a stable limit cycle) and thus periodic plane waves are formed.

It is interesting to note that the underlying kinetics also have a stable limit cycle when $p = 0.24326$ or $p = 0.24327$ and thus one might expect to observe regular periodic plane waves in these cases also. However, Fig. 14 shows that this is not the case. The reasons for this are not clear. It appears that the traveling wave prefers to follow branch A of homoclinic orbits whenever it can, thus leading to the appearance of secondary waves and irregular behavior, and it is not until branch A disappears at the T-point that the waves are governed by the underlying stable limit cycle.

In conclusion, our numerical evidence shows that branch A of homoclinic orbits is the one that generates physiologically significant traveling waves. The speed of the waves increases with increasing p (as has been observed experimentally in many cell types) and there is region of parameter space where the waves become irregular. If p is too low traveling waves fail to exist, as the lower part of branch A denotes waves that are unstable.

4.2 Waves in the three-state model

Waves in the three-state model have a similar qualitative behavior to those discussed above, although the extra dimension (4 instead of 3) makes the behavior more difficult to visualise, and allows for a greater range of possibilities.

4.2.1 The branch of Hopf bifurcations

As before, we draw the curve of Hopf bifurcations in the p, s plane, to get the curve labelled HB in Fig. 15. There is no no loop at the bottom of the curve, as the curve of steady states now has no limit points (cf. Fig. 3).

As before, for each fixed value of s, we can track the branch of periodic orbits arising from the two Hopf bifurcations. For intermediate values of s, the periodic orbits arising from the right-hand branch of HB terminates in a homoclinic bifurcation (HC), while the periodic orbits arising from the left-hand branch of HB terminates in a periodic orbit, in a manner that we describe shortly.

4.2.2 The homoclinic branch

The homoclinic branch now does not end in a T-point, as it did in the two-state model. (Of course, the T-point cannot exist in this model, as there are no limit points in the steady-state curve, and thus there is a single steady state for all values of p). Instead, it bends around in a turning point, TP, and forms a complicated loop of homoclinic orbits (not shown in detail here). This is not obvious from Fig. 15, as the loops all lie so close to one another that the HC branch appears as a single curve. However, a more detailed inspection shows that, as one moves along the branch and goes around the turning point, the homoclinic orbits develop multiple peaks. In Fig. 16A we show two homoclinic orbits on the branch, before TP is reached. The approximated position where these homoclinic orbits appear on the HC branch is indicated by the labeled crosses in Fig. 15. Note that orbit 2 is closer to TP than is orbit 1. As the homoclinic orbits get closer to TP they start developing a smaller trailing peak. As the homoclinic orbits pass around the turning point, they become double-peaked (orbit 3, shown in Fig. 16B). We conjecture that, as the HC branch develops more folds, each additional fold leads to additional peaks in the homoclinic orbits. The existence of multiple-peak

traveling wave solutions has been studied extensively in simpler models (Hastings, 1982; Evans *et al.*, 1982; Feroe, 1982; Glendinning, 1987). The ones we find here by numerical solution of the ODEs do not appear to be stable solutions of the PDEs.

It is helpful to look at the bifurcation occuring at TP in another way by fixing s either above or below the value at TP, and looking at the amplitude and period of the branches of periodic orbits arising for that fixed value of s. Let s_t denote the value of s at the turning point, TP. When $s > s_t$, the two Hopf bifurcations are connected by a single branch of periodic orbits, as illustrated in Fig. 17A, where we used the value $s = 5.4$. The lower Hopf bifurcation is subcritical. At $s = s_t$, the branch of periodic orbits breaks into two separate branches, A and B, one of which (A) now ends in a homoclinic bifurcation on the HC branch, as discussed above. A typical example of this is shown in Fig. 17B, where we used the value $s = 5.2$.

The behaviour of branch B of periodic orbits is also interesting. Along branch B, the period tends to infinity in a series of loops (see the right panel of Fig. 17B), and each loop appears to correspond to the formation of additional peaks in the periodic orbit. Two examples of periodic orbits on branch B are shown in Fig. 18, labeled 5 and 6. Curve 5 has period 425, while curve 6 has period 743. As can be seen from the figure, curve 5 agrees well with the first 453 seconds of curve 6, but then curve 6 develops additional peaks that are not present in curve 5. These additional peaks are made possible by the increased period of curve 6. As the period increases, further peaks continue to appear, but they all appear with a period of 81.4. Hence, as the period tends to infinity, branch B of periodic orbits tends towards the periodic orbit of period 81.4 that occurs at the place where the two branches of periodic orbits intersect (labeled 4 in Fig. 17B). In effect, as the period increases, the periodic orbit develops more and more turns around the steady state, until, at point 4, all these turns collapse onto the simple limit cycle of period 81.4 that occurs on branch A. To illustrate this, we include in Fig. 18 the periodic orbit occuring at point 4 on branch A (dotted line). Clearly, orbit 4 agrees well with orbit 6, differing only in the middle portion of the orbit. (The phases are slightly different for larger times, but this doesn't affect the phase-plane structure.)

4.2.3 Waves in the three-state model PDEs

Numerical solution of the model PDEs (using the same procedure as described above) shows that the stable traveling wave of the PDE corresponds to a homoclinic orbit on HC branch A (Fig. 19A). The other homoclinic orbits in the traveling wave equations appear to correspond to waves that are unstable wave solutions of the PDEs, although we have not checked this in all cases. In the three-state model the wave speed and amplitude are less than in the two-state model, probably because of a decrease in excitability due to the additional time delays introduced by the third variable. As the homoclinic orbit approaches the turning point, TP, secondary waves are introduced (Fig. 19B), just as in the two-state model, except that now the secondary waves travel only in a single direction. The reason for this is not clear, but seems to be a result of the slower initiation of the secondary wave. Hence, we don't see the same type of disordered behavior that was seen in the two-state model. As expected, once p increases past the turning point, the waves become periodic (computations not shown).

5 Summary and Conclusions

Based on the ideas of Hajnóczky and Thomas (1997) and Cardy *et al.* (1997), we have constructed a new model of the IP_3 receptor. In this model, Ca^{2+} modulates the binding affinity of IP_3 to its receptor, and thus oscillations and waves of intracellular Ca^{2+} concentration arise from the sequential binding and unbinding of IP_3 to the receptor. The model is designed particularly to model ACh-induced oscillations and waves in pancreatic acinar cells, and a simplified version is discussed in more detail in LeBeau *et al.* (submitted).

The full three-state model can be reduced to a two-state model by assuming the fact activation of the IP_3 receptor by Ca^{2+}, and the overall qualitative behavior is retained. We have performed a detailed numerical bifurcation analysis of waves in both the two-state and three-state models. Isolated traveling waves in both models arise in a qualitatively similar fashion, being the result of a homoclinic bifurcation in a branch of periodic orbits that arise, in turn, from Hopf bifurcations. Although the structure of the possible waves is extremely complicated, numerical studies suggest that only a single branch is stable, and thus of physiological interest. Along this branch, the wave

speed increases as a function of the bifurcation parameter, p, which corresponds to the background concentration of IP_3. This result is consistent with previous theoretical work on calcium wave propagation (Sneyd *et al.*, 1993; Jafri, 1995), and with the available experimental evidence (Nathanson *et al.*, 1992). One particularly interesting prediction arising from the present work is the occurrence of secondary traveling waves that can be caused by the trailing tail of the primary wave. In the two-state model the physiologically significant branch of homoclinic orbits ends in a T-point, a heteroclinic cycle, and a spiral branch of homoclinic orbits. This heteroclinic cycle causes the appearance of secondary waves behind the primary wave. These secondary waves can travel in a direction opposite to that of the primary wave, and can themselves generate tertiary waves, and so on. In certain parameter regimes, this can lead to disordered wave activity, reminiscent of spatio-temporal chaos.

Here, we have concentrated on studying the wave behavior in the non-oscillatory, excitable, regime. It is of equal importance to study the types of stable periodic waves that occur in the oscillatory regime (roughly, between the Hopf bifurcations) but this is left for future work.

Acknowledgements

We thank Neil Balmforth for helping us to identify the T-point. James Sneyd was supported by NIGMS grant R01 GM56126, and NSF grant DMS 9706565. David Yule was supported by NIDDK grant R01 DK54568.

References

Atri, A., J. Amundson, D. Clapham and J. Sneyd, (1993) A single-pool model for intracellular calcium oscillations and waves in the *Xenopus laevis* oocyte, *Biophysical Journal.* 65: 1727–1739.

Balmforth, N. J., G. R. Ierley and E. A. Spiegel, (1994) Chaotic pulse trains, *SIAM Journal on Applied Mathematics.* 54: 1291–1334.

Bezprozvanny, I. and B. E. Ehrlich, (1995) The inositol 1,4,5-trisphosphate ($InsP_3$) receptor, *J. Membrane Biol..* 145: 205–216.

Cardy, T. J., D. Traynor and C. W. Taylor, (1997) Differential regulation of types-1 and -3 inositol trisphosphate receptors by cytosolic Ca^{2+}, *Biochem. J..* 328: 785–793.

Doedel, E., *Software for continuation and bifurcation problems in ordinary differential equations*: California Institute of Technology, 1986.

Dufour, J.-F., I. M. Arias and T. J. Turner, (1997) Inositol 1,4,5-trisphosphate and calcium regulate the calcium channel function of the hepatic inositol 1,4,5-trisphosphate receptor, *The Journal of Biological Chemistry.* 272: 2675–2681.

Evans, J. W., N. Fenichel and J. A. Feroe, (1982) Double impulse solutions in nerve axon equations, *SIAM Journal on Applied Mathematics.* 42: 219–234.

Feroe, J. A., (1982) Existence and stability of multiple impulse solutions of a nerve equation, *SIAM Journal on Applied Mathematics.* 42: 235–246.

Finch, E. A., T. J. Turner and S. M. Goldin, (1991) Calcium as a coagonist of inositol 1,4,5-trisphosphate-induced calcium release, *Science.* 252: 443–446.

Glendinning, P. and C. Sparrow, (1984) Local and global behavior near homoclinic orbits, *Journal of Statistical Physics.* 35: 645–696.

Glendinning, P. and C. Sparrow, (1986) T-points: A codimension two heteroclinic bifurcation, *Journal of Statistical Physics.* 43: 479–488.

Glendinning, P., (1987) Travelling wave solutions near isolated souble-pulse solitary waves of nerve axon equations, *Physics Letters A.* 121: 411–413.

Hajnóczky, G. and A. P. Thomas, (1997) Minimal requirements for calcium oscillations driven by the IP_3 receptor, *Embo J.* 16: 3533–3543.

Hastings, S. P., (1982) Single and multiple pulse waves for the FitzHugh-Nagumo equations, *SIAM Journal on Applied Mathematics.* 42: 247–260.

Jafri, M. S. and J. Keizer, (1994) Diffusion of inositol 1,4,5-trisphosphate, but not Ca^{2+}, is necessary for a class of inositol 1,4,5-trisphosphate-induced Ca^{2+} waves, *Proc. Natl. Acad. Sci. (USA).* 91: 9485–9489.

Jafri, M. S., (1995) A theoretical study of cytosolic calcium waves in *Xenopus* oocytes, *Journal of Theoretical Biology.* 172: 209–216.

Kaftan, E. J., B. E. Ehrlich and J. Watras, (1997) Inositol 1,4,5-trisphosphate ($InsP_3$) and calcium interact to increase the dynamic range of $InsP_3$ receptor-dependent calcium signaling, *J. Gen. Physiol..* 110: 529–538.

Kasai, H., (1995) Pancreatic calcium waves and secretion, *Ciba Found Symp.* 188: 104-16.

Keizer, J. and G. DeYoung, (1994) Simplification of a realistic model of IP_3-induced Ca^{2+} oscillations, *J. Theor. Biol..* 166: 431–442.

Lawrie, A. M., E. C. Toescu and D. V. Gallacher, (1993) Two different spatiotemporal patterns for Ca^{2+} oscillations in pancreatic acinar cells: evidence of a role for protein kinase C in Ins(1,4,5)P_3-mediated Ca^{2+} signalling, *Cell Calcium.* 14: 698–710.

Li, Y.-X. and J. Rinzel, (1994) Equations for $InsP_3$ receptor-mediated [Ca^{2+}] oscillations derived from a detailed kinetic model: a Hodgkin-Huxley like formalism, *J. Theor. Biol..* 166: 461–473.

Maginu, K., (1985) Geometrical characteristics associated with stability and bifurcations of periodic travelling waves in reaction-diffusion equations, *SIAM Journal of Applied Mathematics.* 45: 750–774.

Nathanson, M. H., P. J. Padfield, A. J. O'Sullivan, A. D. Burgstahler and J. D. Jamieson, (1992) Mechanism of Ca^{2+} wave propagation in pancreatic acinar cells, *J Biol Chem.* 267: 18118-21.

Parys, J. B., S. W. Sernett, S. DeLisle, P. M. Snyder, M. J. Welsh and K. P. Campbell, (1992) Isolation, characterization, and localization of the inositol 1,4,5-trisphosphate receptor protein in *Xenopus laevis* oocytes, *Journal of Biological Chemistry.* 267: 18776–18782.

Petersen, C. C. H., E. C. Toescu and O. H. Petersen, (1991) Different patterns of receptor-activated cytoplasmic Ca^{2+} oscillations in single pancreatic acinar cells: dependence on receptor type, agonist concentration and intracellular Ca^{2+} buffering, *EMBO Journal.* 10: 527–533.

Pfeiffer, F., L. Sternfeld, A. Schmid and I. Schulz, (1998) Control of Ca^{2+} wave propagation in mouse pancreatic acinar cells, *Am J Physiol.* 274: C663-72.

Sil'nikov, L. P., (1965) A case of the existence of a denumerable set of periodic motions, *Sov. Math. Dokl..* 6: 163–166.

Sneyd, J., S. Girard and D. Clapham, (1993) Calcium wave propagation by calcium-induced calcium release: an unusual excitable system, *Bulletin of Mathematical Biology.* 55: 315–344.

Sneyd, J., J. Keizer and M. J. Sanderson, (1995) Mechanisms of calcium oscillations and waves: a quantitative analysis, *FASEB Journal.* 9: 1463–1472.

Sneyd, J., P. Dale and A. Duffy, (1998) Traveling waves in buffered systems: applications to calcium waves, *SIAM J. Appl. Math.* 58: 1178–1192.

Tang, Y., J. L. Stephenson and H. J. Othmer, (1996) Simplification and analysis of models of calcium dynamics based on IP_3-sensitive calcium channel kinetics., *Biophysical Journal.* 70: 246–263.

Thomas, A. P., G. S. J. Bird, G. Hajnóczky, L. D. Robb-Gaspers and J. W. J. Putney, (1996) Spatial and temporal aspects of cellular calcium signaling, *FASEB Journal.* 10: 1505–1517.

Thorn, P., A. M. Lawrie, P. M. Smith, D. V. Gallacher and O. H. Petersen, (1993) Ca^{2+} oscillations in pancreatic acinar cells: spatiotemporal relationships and functional implications, *Cell Calcium.* 14: 746–757.

Wagner, J. and J. Keizer, (1994) Effects of rapid buffers on Ca^{2+} diffusion and Ca^{2+} oscillations, *Biophysical Journal.* 67: 447–456.

Wiggins, S., *Introduction to Applied Nonlinear Dynamical Systems and Chaos*: Springer, New York, 1990.

Yoneshima, H., A. Miyawaki, T. Michikawa, T. Furuichi and K. Mikoshiba, (1997) Ca^{2+} differentially regulates the ligand-affinity states of type 1 and type 3 inositol 1,4,5-trisphosphate receptors, *Biochem. J.*. 322: 591–596.

Yule, D. I., A. M. Lawrie and D. V. Gallacher, (1991) Acetylcholine and cholecystokinin induce different patterns of oscillating calcium signals in pancreatic acinar cells, *Cell Calcium.* 12: 145–151.

Yule, D. I., E. Stuenkel and J. A. Williams, (1996) Intercellular calcium waves in rat pancreatic acini: mechanism of transmission, *American Journal of Physiology (Cell Physiol.).* 271: C1285–C1294.

Figure Captions

Figure 1: Schematic diagram of the receptor model of LeBeau *et al.* (submitted).

Figure 2: A: Schematic diagram of the full receptor model. B: reduction of the full model by assuming fast calcium binding leads to this simplified binding diagram, a slightly generalised version of the one shown in Fig. 1.

Figure 3: Bifurcation diagram of the three-state model, showing the maximum and minimum of the periodic orbit as a function of p. The inset shows the period of the periodic orbit as a function of p. HB – Hopf bifurcation.

Figure 4: Bifurcation diagram of the two-state model, showing the maximum and minimum of the periodic orbit as a function of p. The inset shows the period of the periodic orbit as a function of p. HB – Hopf bifurcation; HC – homoclinic bifurcation. A broken line denotes instability.

Figure 5: A: Two-parameter bifurcation diagram of the traveling wave equations of the two-state model. HB denotes the curve of Hopf bifurcations, and HC denotes the branches of homoclinic bifurcations. LP denotes a limit point. For values of p between the two limit points there are three steady states. The numbered crosses correspond to homoclinic orbits that are plotted in later figures. B: magnified view of the homoclinic spiral and T-point. C: magnified view of LP2, and the lower part of HC branch C.

Figure 6: Bifurcation diagram of the traveling wave equations of the two-state model, for a fixed value of $s = 12$. Solid curve denotes the maximum and minimum values of c over a periodic orbit, and the dashed curve denotes a curve of steady states. Stability is not indicated. The inset shows the period of the two branches of periodic orbits. HB – Hopf bifurcation. HC – homoclinic bifurcation.

Figure 7: Homoclinic orbits from the labeled points in Fig. 5A and B. As mentioned in the text, these are not true homoclinic orbits, merely orbits of period 10,000 (for convenience scaled to have period 1 here). Orbits with period 1,000 look exactly the same, and thus these orbits are close approximations to the true homoclinic orbit. The same is true for all the homoclinic orbits shown here.

Figure 8: The heteroclinic cycle at the T-point. A: view of whole cycle. B: magnified view of the cycle in the vicinity of the saddle-point (SP) and the saddle-focus (SF).

Figure 9: Homoclinic orbits from the labeled points in Fig. 5A and B.

Figure 10: Homoclinic orbits from the labeled points in Fig. 5A and C.

Figure 11: Bifurcation diagrams for three fixed values of s close to LP1. Solid curves denote the maxima and minima of the periodic orbits. Dashed curves denote the curves of steady states. Right-hand panels show the period of the branches of periodic orbits.

Figure 12: Homoclinic orbits from the labeled points in Fig. 5A and C.

Figure 13: Solitary wave solutions of the two-state model, obtained by direct numerical simulation of the PDEs for three different values of p. For higher values of p, the solitary wave develops a trailing secondary wave as described in the text.

Figure 14: Wave solutions of the two-state model, obtained by direct numerical simulation of the PDEs, and plotted in the space-time plane. For higher values of p, the waves become periodic.

Figure 15: A: Two-parameter bifurcation diagram of the traveling wave equations of the three-state model. HB denotes the curve of Hopf bifurcations, and HC denotes the branch of homoclinic bifurcations. TP denotes the turning point, where the branch of homoclinic bifurcations folds up. Labeled points correspond to homoclinic orbits shown in later figures.

Figure 16: Homoclinic orbits from the labeled points in Fig. 15. Curve 3 is from the homoclinic branch after it has passed around the turning point, TP, and has thus developed an additional peak, as described in the text.

Figure 17: Bifurcation diagram of the three-state model, for two different values of s on either side of the turning point. Labeled points correspond to periodic orbits shown in the next figure.

Figure 18: Three periodic orbits corresponding to the labeled points in the previous figure. As the two branches of periodic orbits merge, the infinite-period orbit of branch B collapses into the finite-period orbit of branch A, as all the loops of the infinite-period orbit coalesce at the bifurcation point.

Figure 19: Wave solutions of the three-state model, obtained by direct numerical simulation of the PDEs. A: solitary wave. B: For higher values of p, the solitary wave gives off trailing secondary waves.

k_f	=	28	J_{leak}	=	0.2
V_p	=	1.2	K_p	=	0.18
k_1	=	0	k_2	=	0.53
k_3	=	1	k_{-1}	=	0.88
r_2	=	100	r_4	=	20
r_6	=	0	r_{-2}	=	0
R_1	=	6	R_3	=	50
R_5	=	1.6	D_c	=	25

Table 1: Sneyd et al.

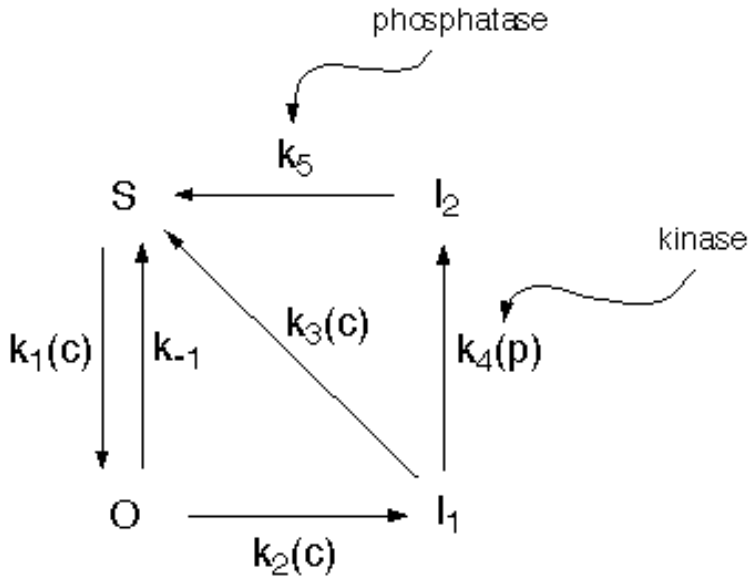

Figure 1: Sneyd et al.

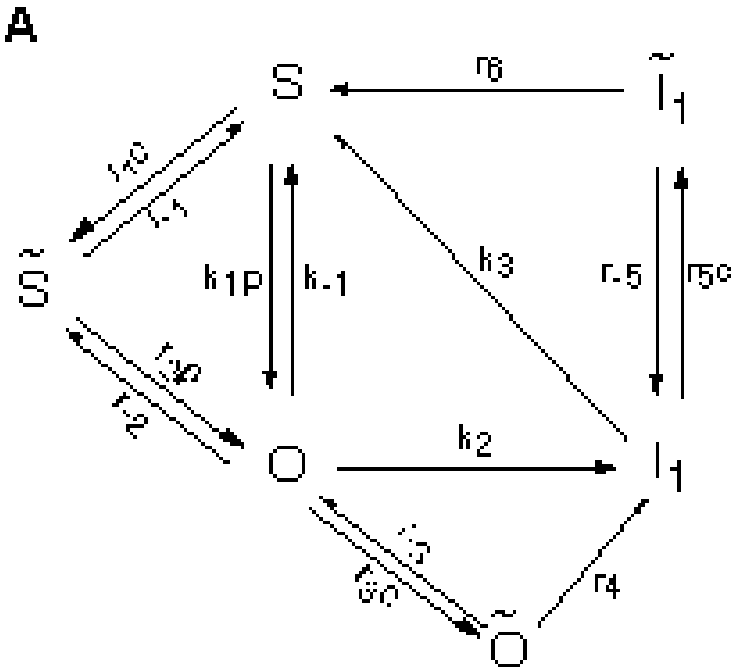

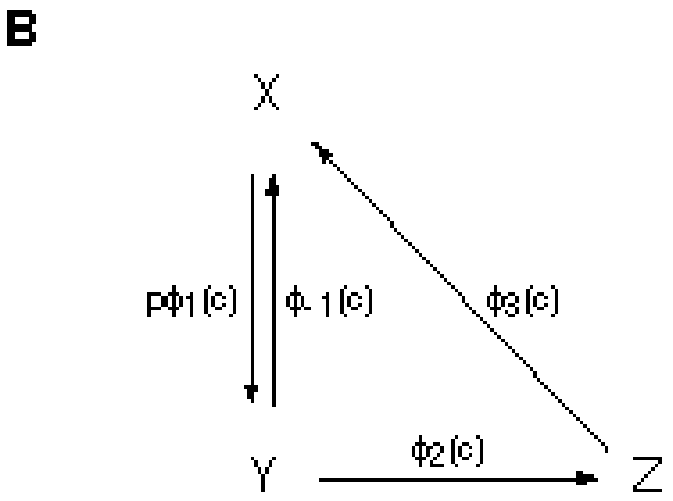

Figure 2: Sneyd et al.

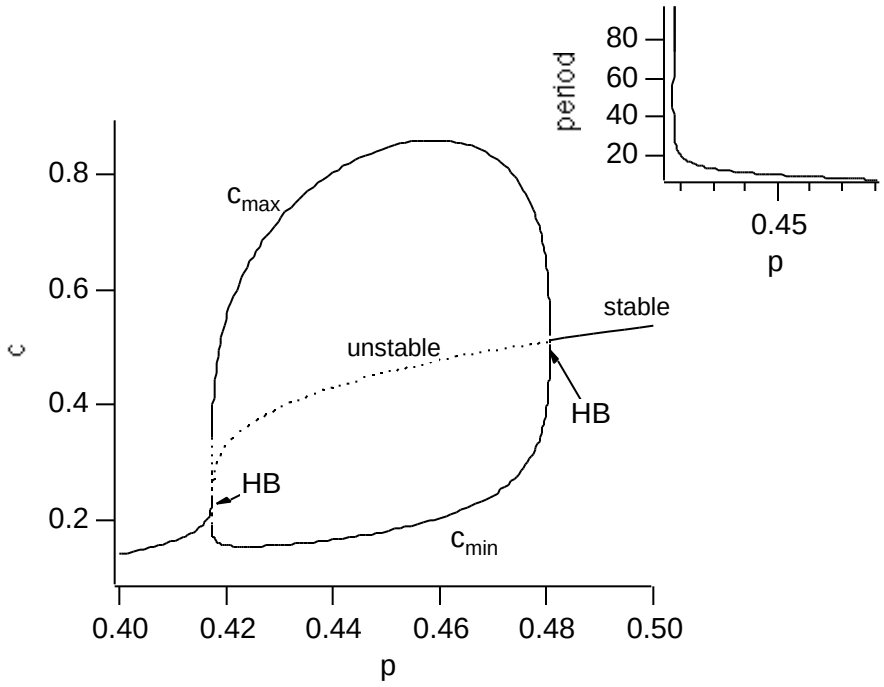

Figure 3: Sneyd et al.

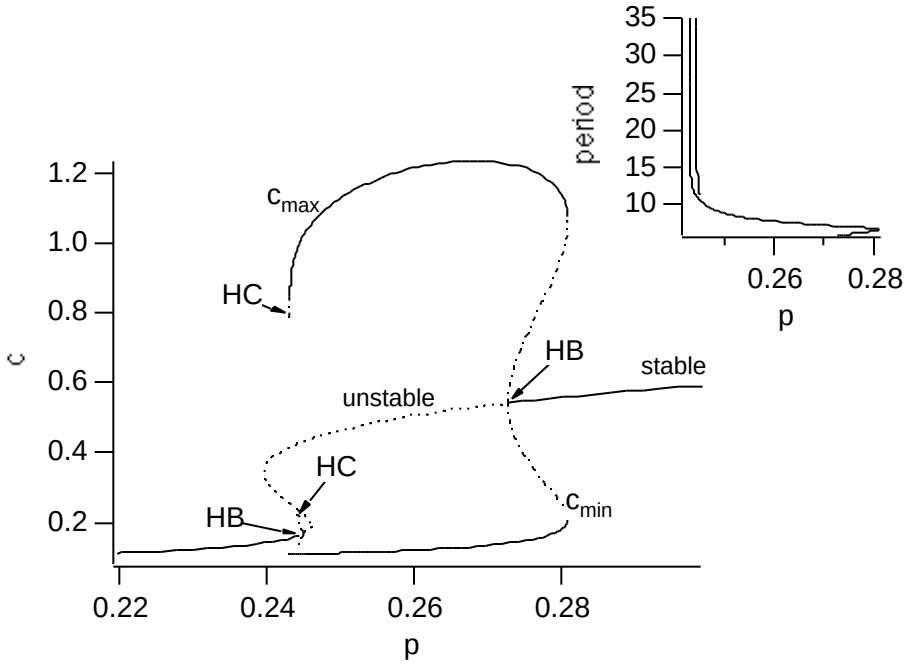

Figure 4: Sneyd et al.

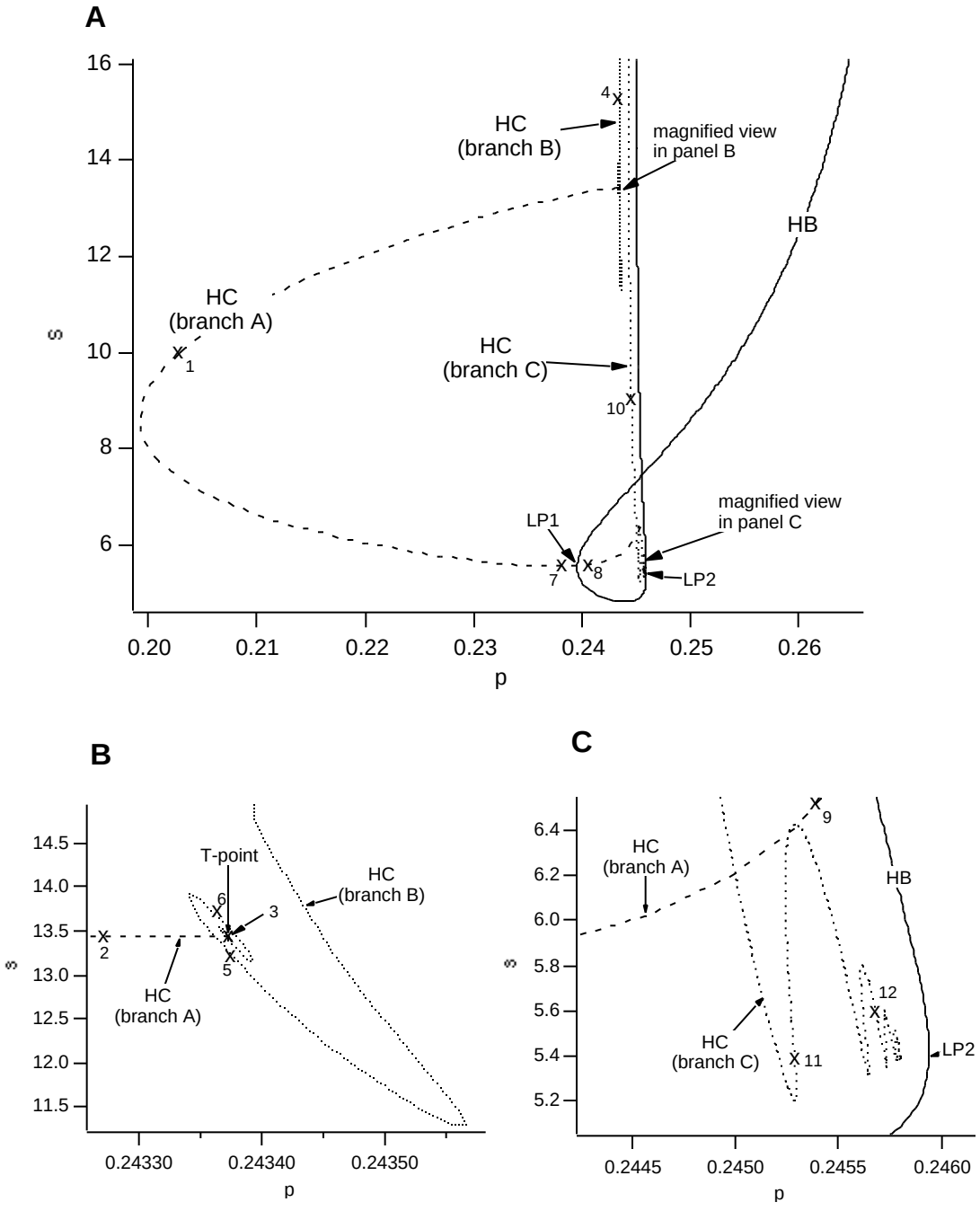

Figure 5: Sneyd et al.

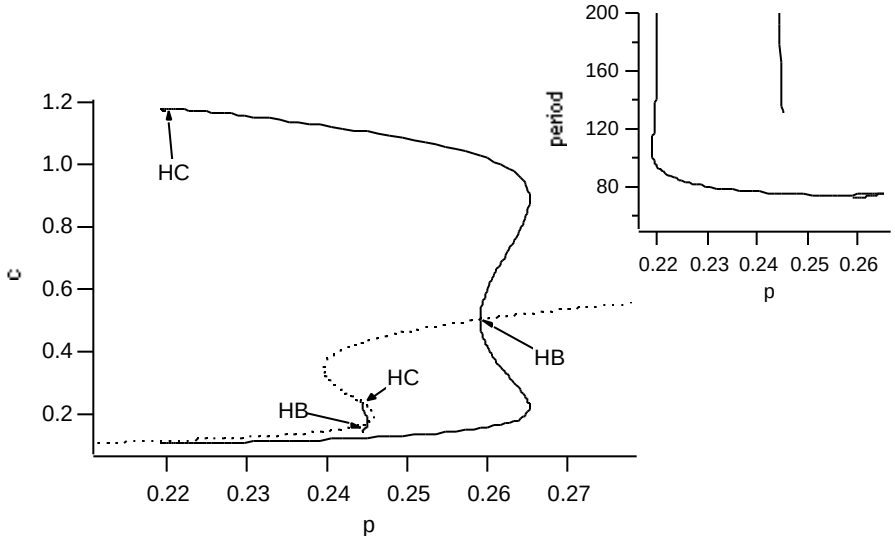

Figure 6: Sneyd et al.

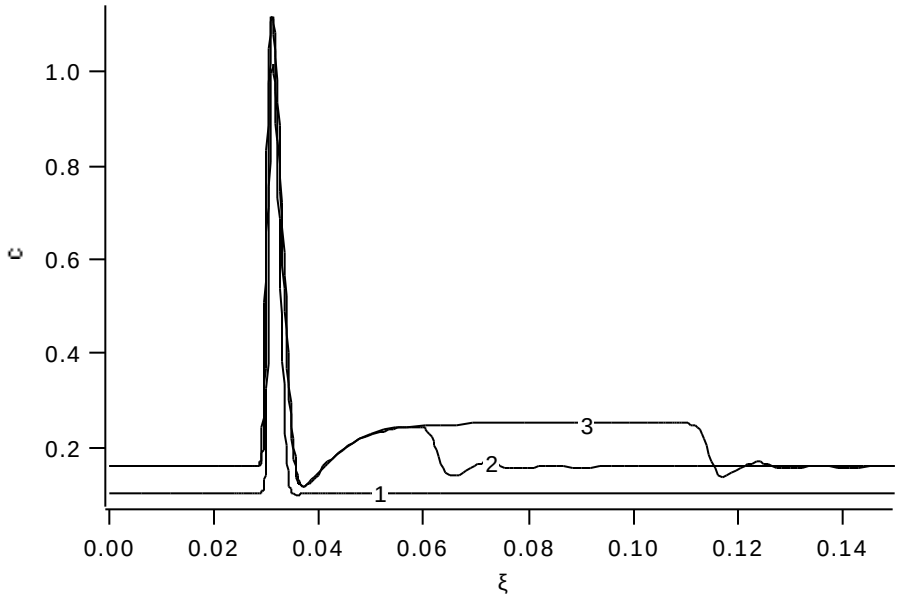

Figure 7: Sneyd et al.

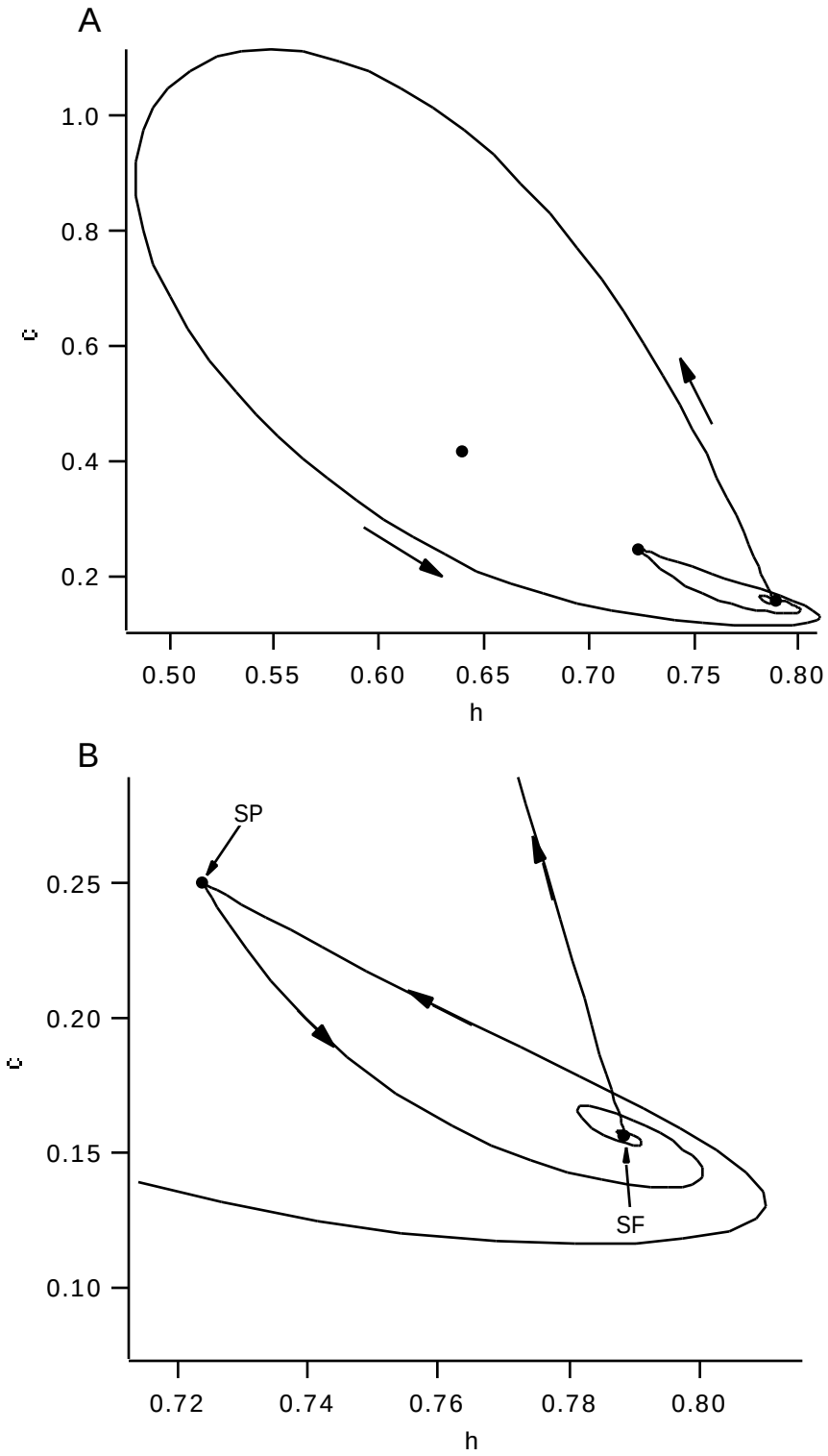

Figure 8: Sneyd et al.

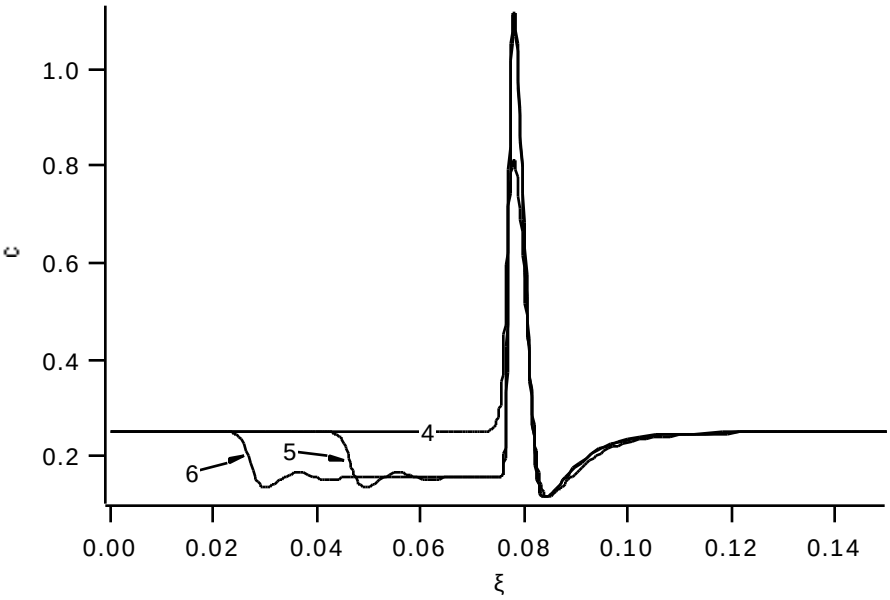

Figure 9: Sneyd et al.

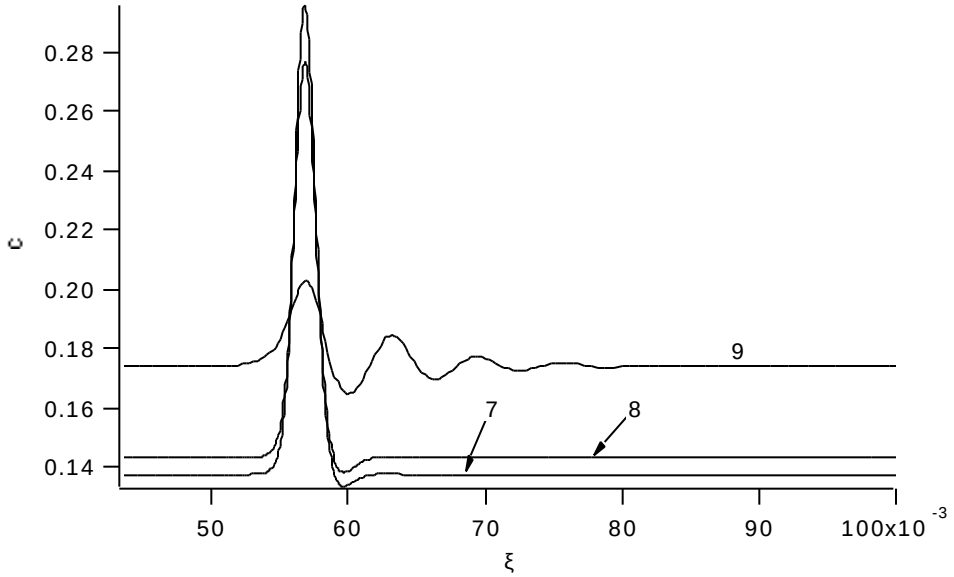

Figure 10: Sneyd et al.

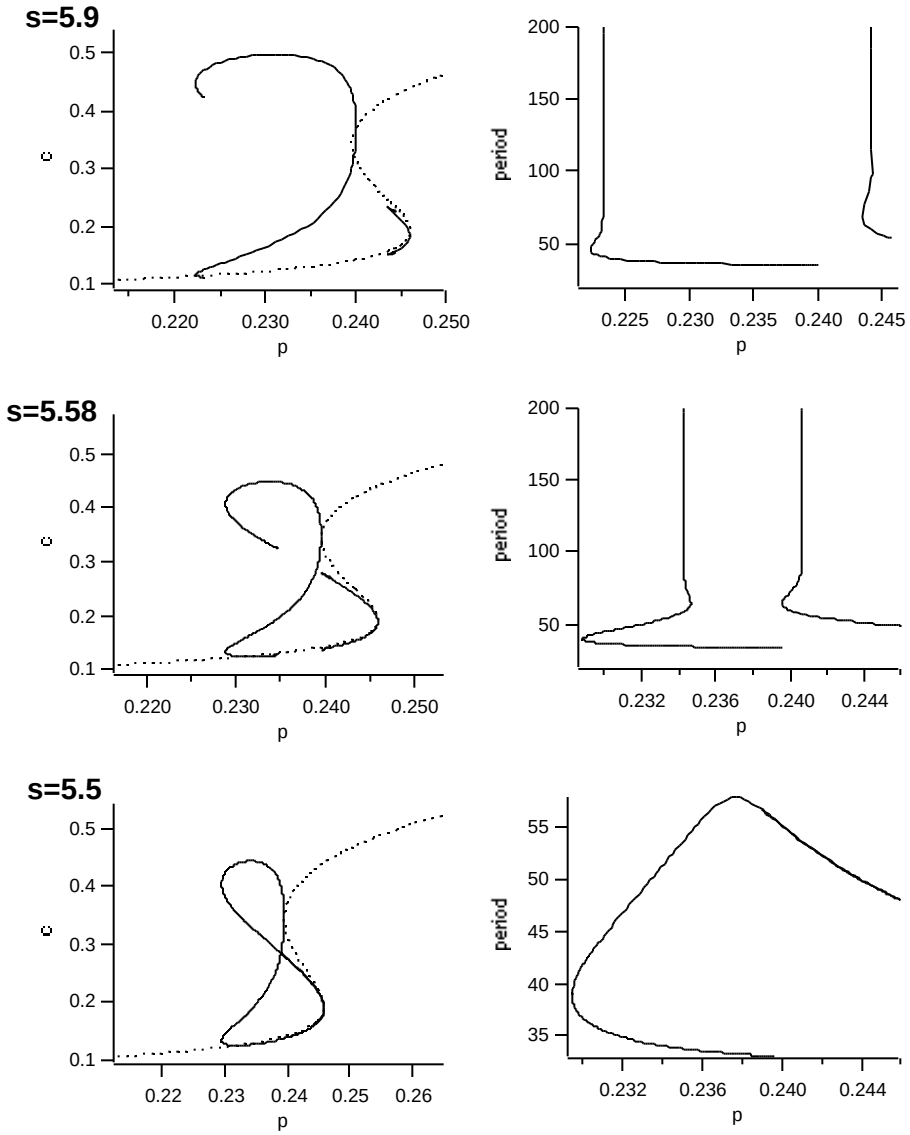

Figure 11: Sneyd et al.

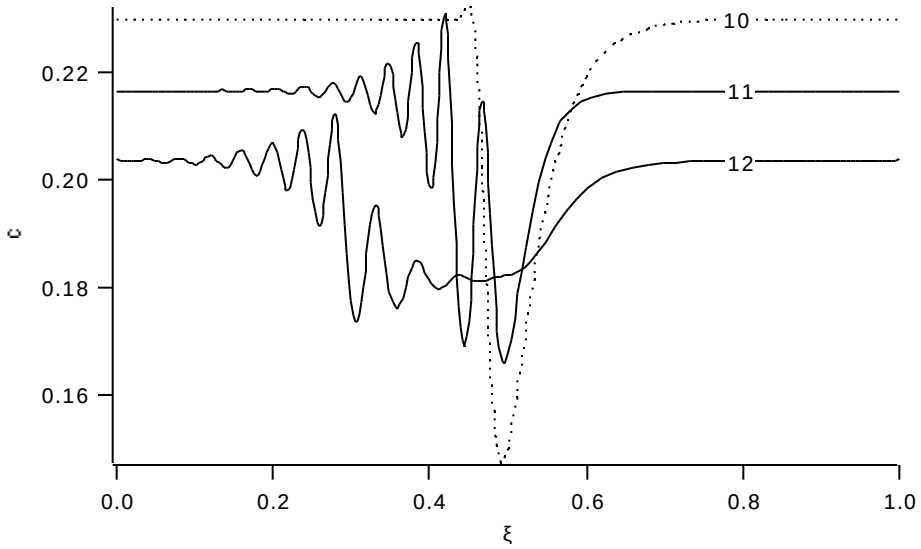

Figure 12: Sneyd et al.

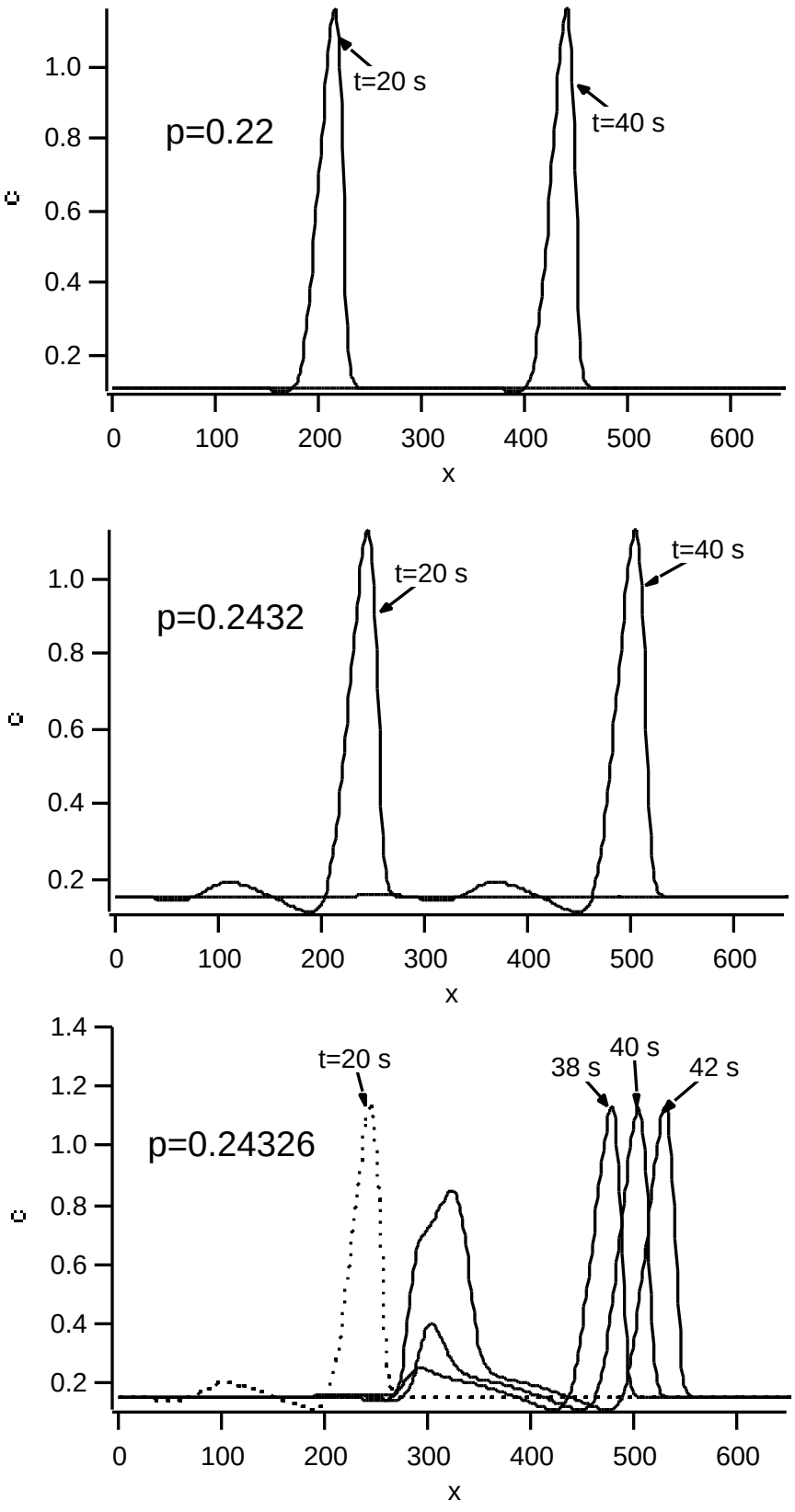

Figure 13: Sneyd et al.

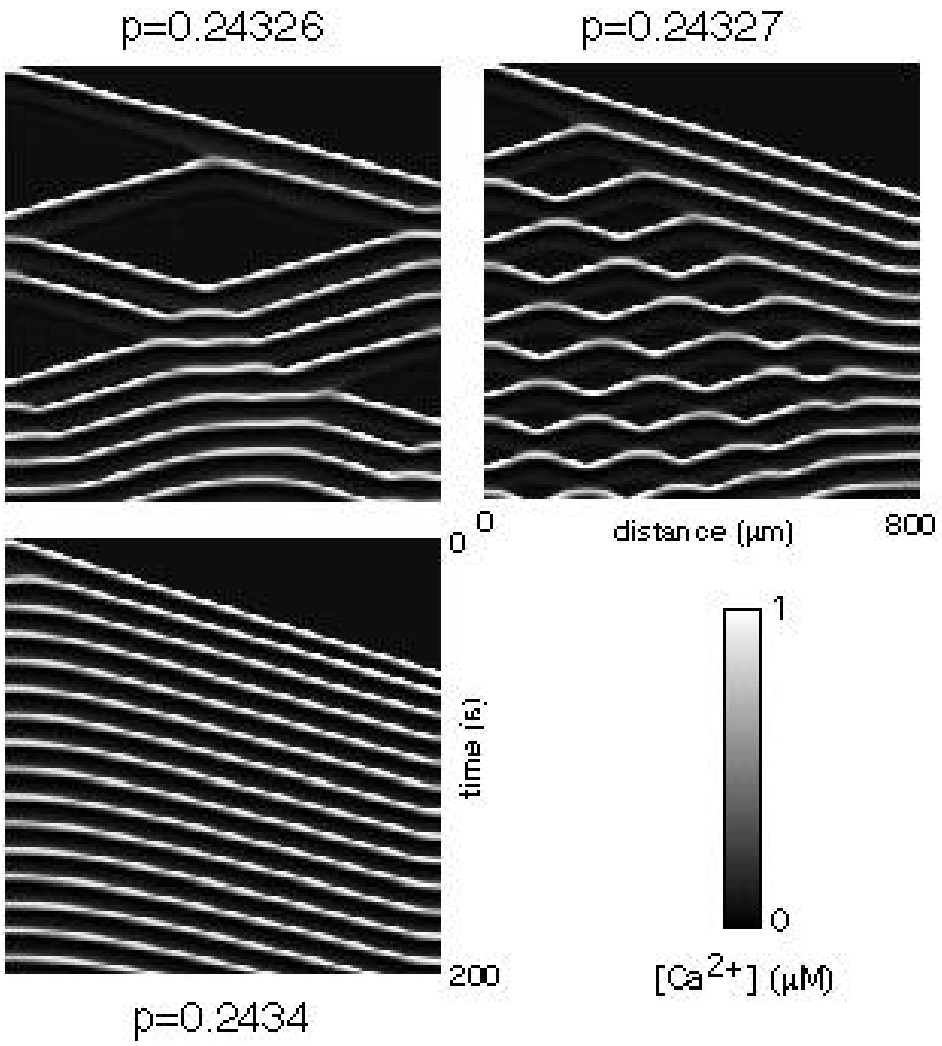

Figure 14: Sneyd et al.

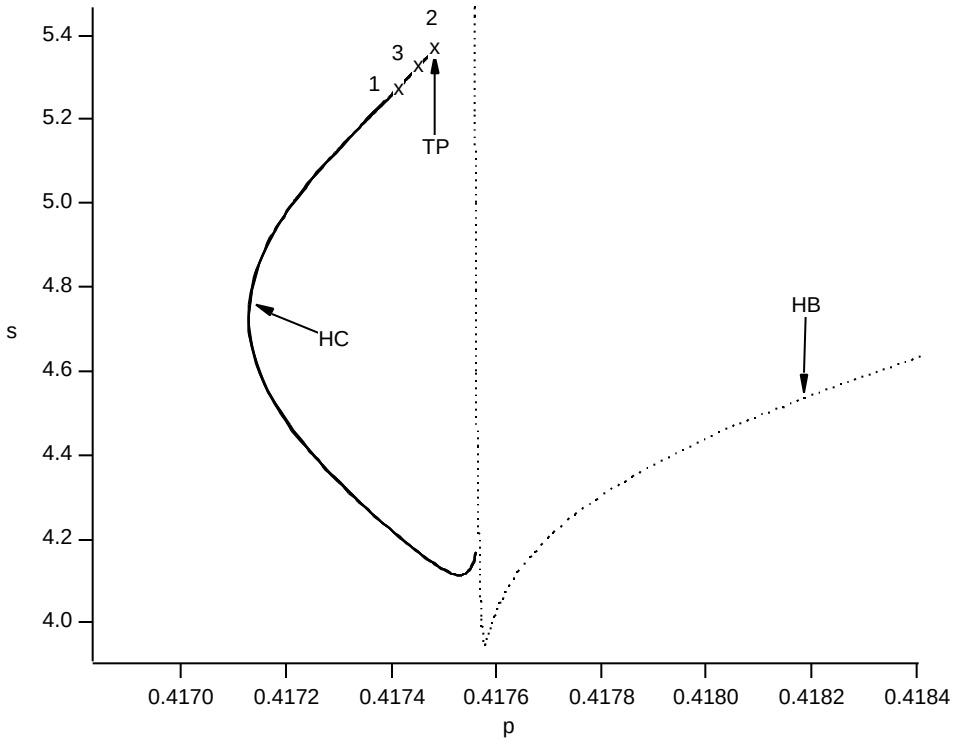

Figure 15: Sneyd et al.

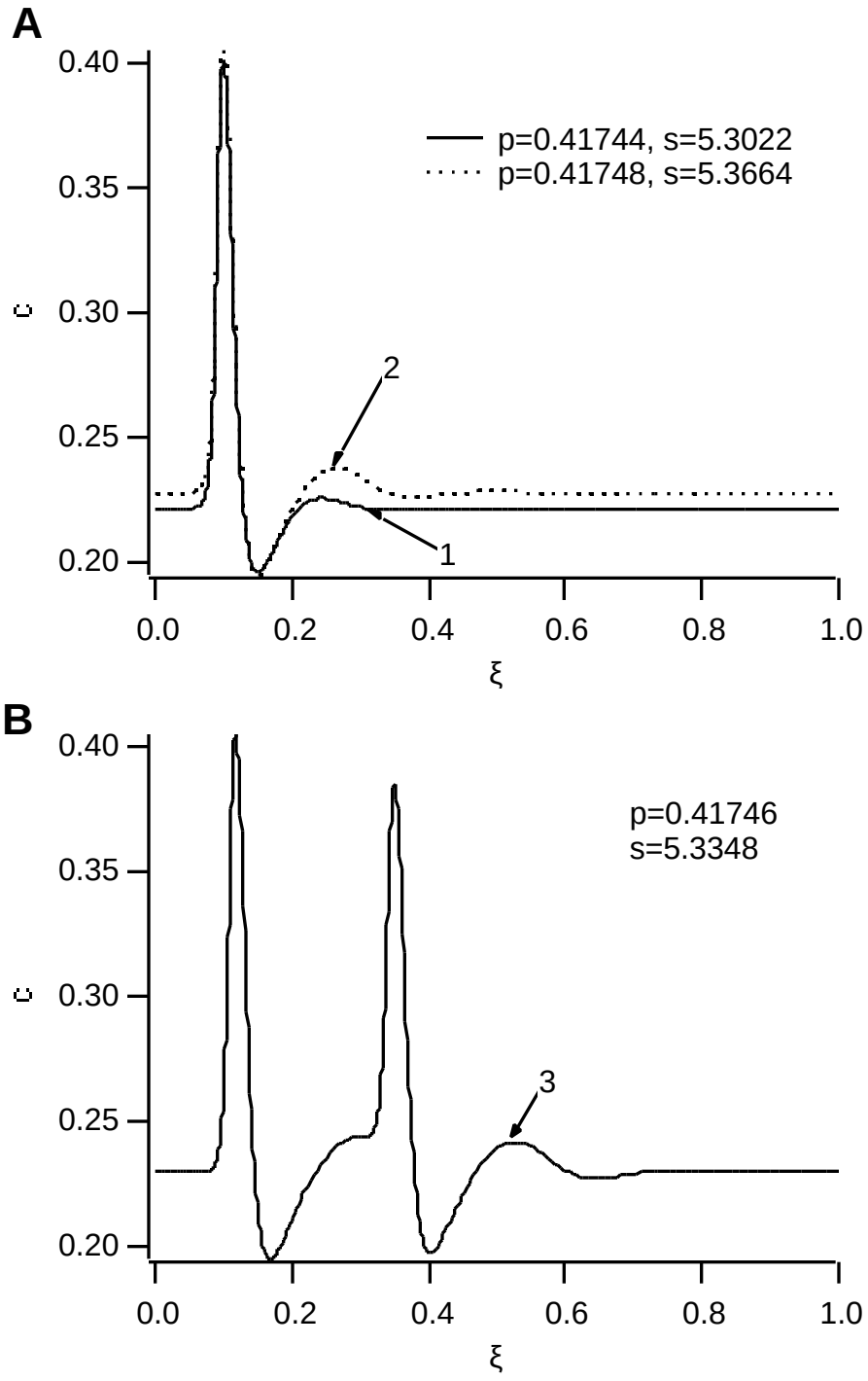

Figure 16: Sneyd et al.

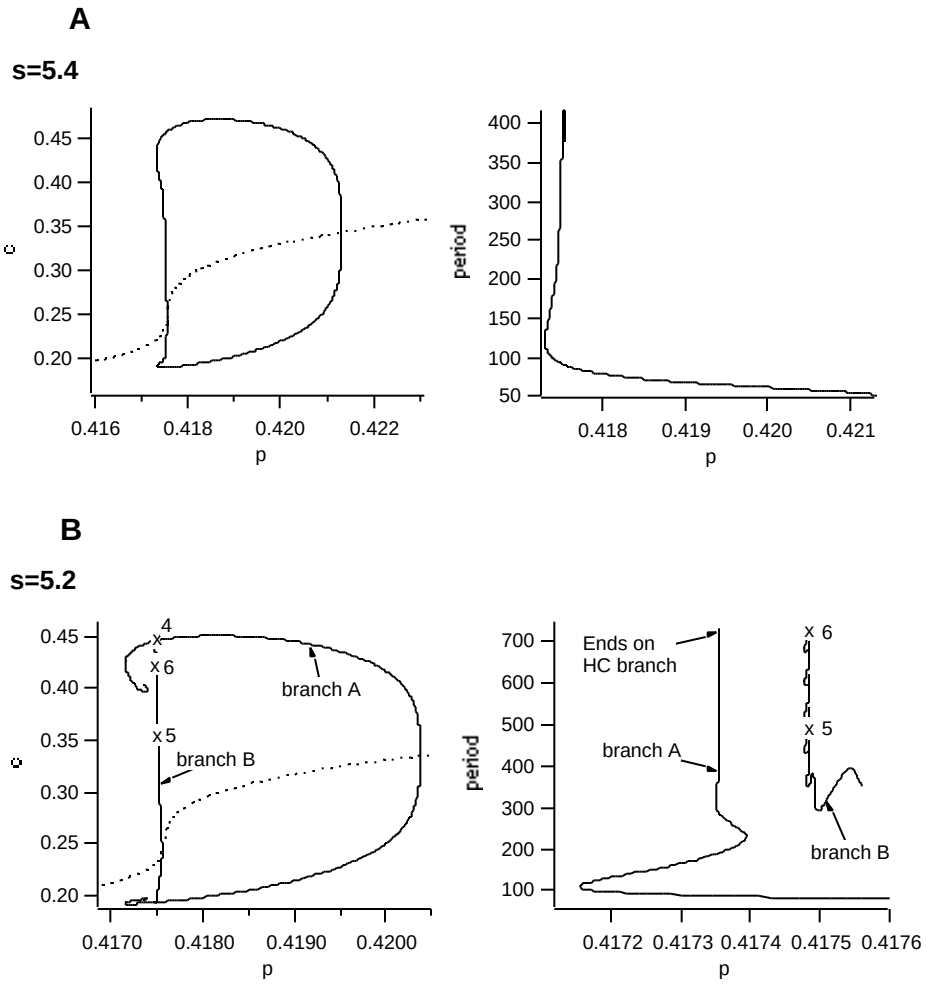

Figure 17: Sneyd et al.

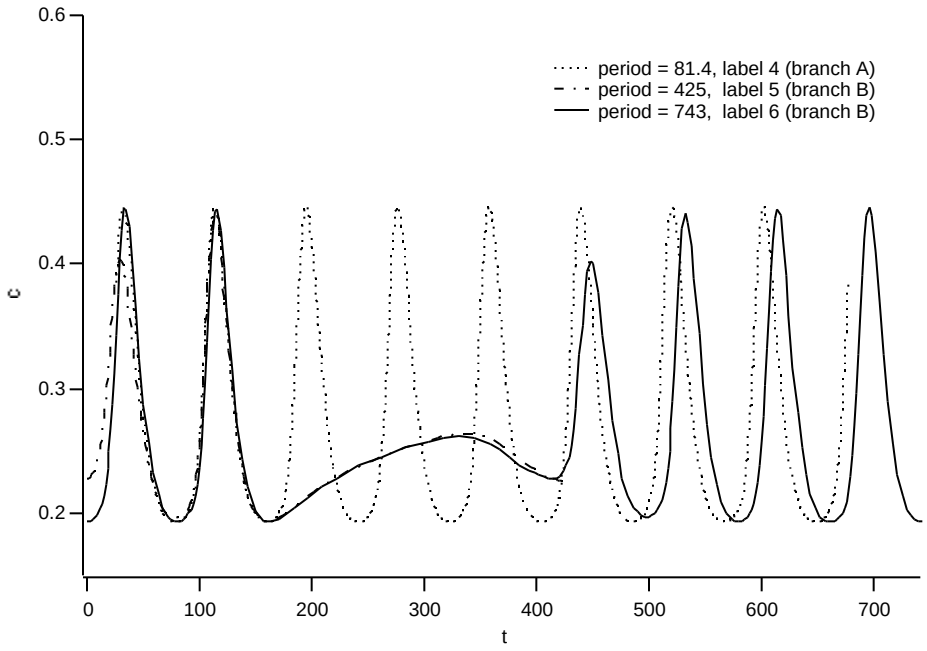

Figure 18: Sneyd et al.

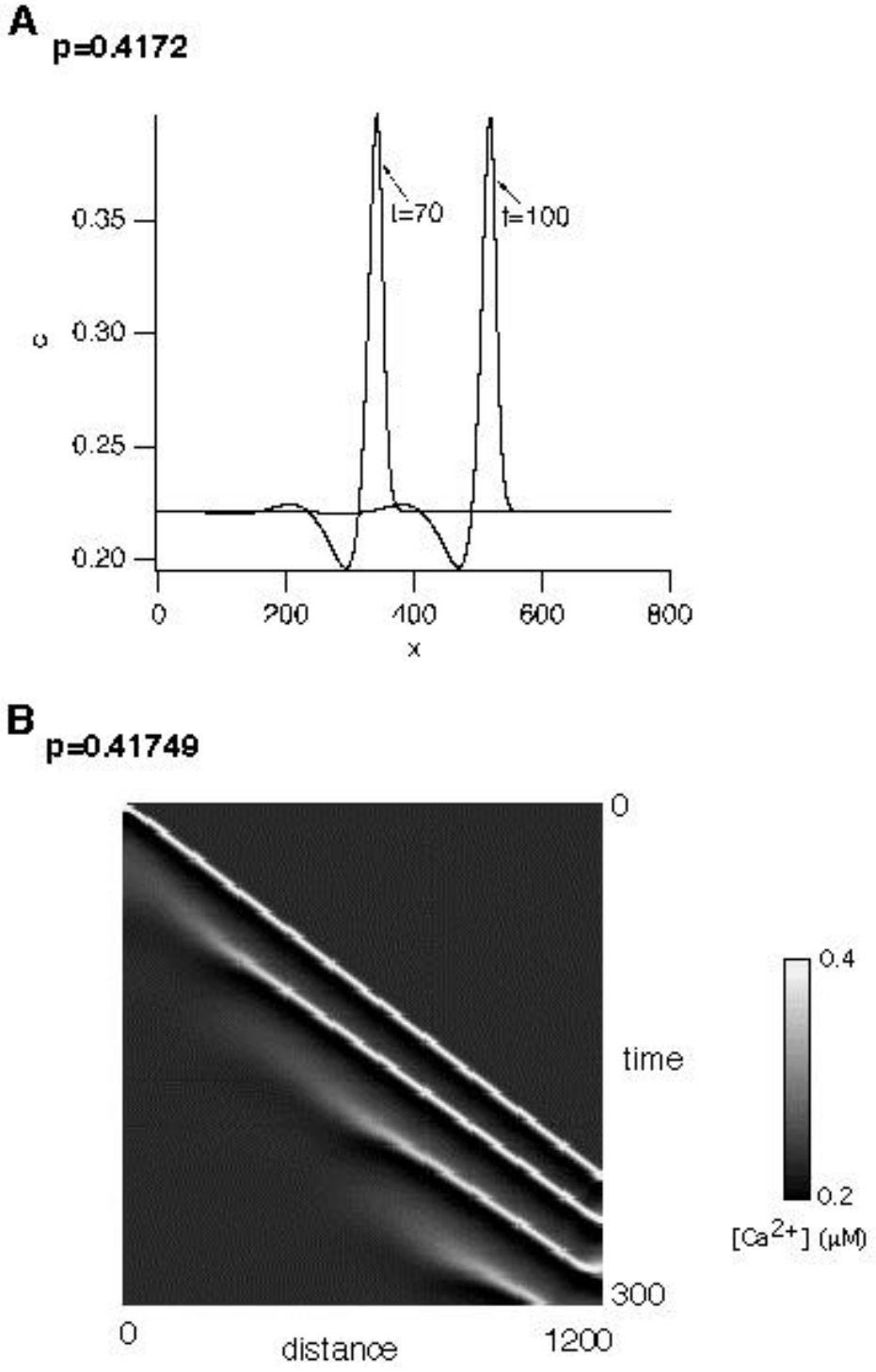

Figure 19: Sneyd et al.